Hindawi
Geofluids
Volume 2023, Article ID 6954611, 15 pages
https://doi.org/10.1155/2023/6954611

Research Article

Study on Stress Evolution and Crushing Behavior of Jointed Rock Mass under Confining Pressure and Joint Materials

Wang Qirui,[1,2] Zhang Qihu,[3] Yang Liyun,[3] Kong Fuli,[2] Ding Chenxi,[4] and Fan Junqi[2]

[1]*Department of Civil Engineering, Tsinghua University, Beijing 100084, China*
[2]*Institute of Defense Engineering, AMS, PLA, Luoyang 471023, China*
[3]*School of Mechanics and Civil Engineering, China University of Mining and Technology (Beijing), Beijing 100083, China*
[4]*School of Civil and Resource Engineering, University of Science and Technology Beijing, Beijing 100083, China*

Correspondence should be addressed to Zhang Qihu; zhang18487084511@163.com

Received 14 December 2022; Revised 11 February 2023; Accepted 18 February 2023; Published 4 March 2023

Academic Editor: Yi Xue

To study the effects of confining pressure and joint material properties on stress evolution and fracture behavior of jointed rock mass under SHPB impact load, the numerical software LS-DYNA and the indoor SHPB impact system are used to carry out experimental research on intact rock mass and jointed rock mass. The peak stress, reflection and transmission coefficient, and specimen failure state of rock specimens under different schemes are obtained. The effects of confining pressure level and joint material properties on the propagation and attenuation law of explosive stress waves are expounded. The test results show that when the confining pressure is within a specific range, the impact resistance of the limestone specimen can be increased, and the more difficult it is to be destroyed. Moreover, if the confining pressure continues to increase after rising to the peak value, the impact resistance of rock specimens will decline. In that case, the impact resistance of the specimen will decrease—the dynamic strength of jointed rock mass changes with a change in joint material. The dynamic strength of cement jointed rock is the highest, that of gypsum jointed rock is the second, and that of epoxy resin jointed rock is the lowest. The impact damage resistance of the jointed rock has the same law as the above.

1. Introduction

The rock mass in mining usually contains defects such as voids, joints, and faults, so the explosion stress waves caused by the explosive explosion will be significantly affected by these defective rock masses [1]. The primary variables that affect the propagation and attenuation of the explosion stress wave are the crack size, joint thickness, joint layer number, and in situ stress level in the structural plane of the rock mass. The rock mass is affected by the explosion nearby in the form of an explosion shock wave. The increased propagation distance will attenuate into the explosion stress wave and continue to propagate outward [2]. When the propagation direction of the explosion stress wave is consistent with the average stress direction of the rock mass structural plane, the stress wave's ability to propagate is weakened by the structural plane, which is conducive to the safety of underground facilities and equipment and protective engineering [3]. It can be seen from the current research that the effect of ground stress on underground engineering has not been fully considered. Through model tests and numerical simulation, the stress evolution and fracture behavior of jointed rock mass under SHPB impact load are studied in relation to confining pressure level and joint material parameters. It has significant theoretical and practical implications for designing underground facility buildings and protective engineering.

Both domestically and internationally, specialists and academics have researched the interplay between stress waves and joint thicknesses, dip angles, number of layers, and other factors from numerical simulation and field tests. The propagation law and change process of stress wave through joints are obtained. Chai et al. [4] used theoretical analysis and numerical simulation methods to perform an in-depth study and analysis of P waves' propagation and attenuation law in nonlinear cross-combination joints. It is

found that the distribution, stiffness, and frequency of incident waves of joints will affect the propagation and attenuation process. Through theoretical derivation and numerical study, Wang et al. [5] elaborated on the energy propagation law and attenuation process of stress wave at the opening of the joint. Ren et al. [6], through numerical simulation software, simulate the propagation process of stress waves in rock masses through joints and intermittent joints. Lu et al. [7] studied and analyzed the propagation and attenuation law of SV waves by numerical simulation, taking the two factors of joint stiffness and inclination as variables. Through field measurement and numerical modeling, Xue et al. [8] investigated and analyzed the propagation and attenuation law of explosion stress waves in various thicknesses, angles, and joints of filler materials. Through numerical modeling, Liu et al. [9] investigated longitudinal wave energy propagation and attenuation law in nonlinear parallel joints. Yu et al. [10] studied wave source parameters, joint parameters, rock mass nonlinearity, joint position, and other parameters through theoretical analysis and numerical calculation. They discussed the influence of dual nonlinear elastic medium of jointed rock mass on transmission wave waveform, transmission coefficient, and wave spectrum distribution. Through theoretical development and numerical investigation, Song et al. [11] examined the impacts of various elements on the law of force wave propagation. They derived the dynamic propagation equation of stress wave vertically incident on jointed rock mass. The jointed rock mass establishes the numerical difference model of stress wave propagation. The theoretical calculation approach for stress wave propagation on discontinuous joint surfaces was developed by Fan et al. [12].

In practical engineering, the stress state of deeply buried jointed rock mass is complex. The stress wave propagates deep underground, coupling with the complex in situ stress. The joint structural plane's geometric characteristics, mechanical properties, and physical morphology significantly impact stress wave propagation. Li et al. [13] studied the propagation attenuation law and failure mode of stress wave in jointed red sandstone through numerical simulation method and SHPB indoor test. Li et al. [14] used granite to make separate SHPB experimental members and carried out stress wave propagation tests on joints containing fillings without considering confining pressure. Zhao et al. [15] conducted ultrasonic wave velocity tests on continuous joints, showing a positive correlation between the wave velocity in the joints and the connection rate of the joints. Liu et al. [16] studied the propagation attenuation law of shear wave propagation caused by the magnitude of normal stress on joint surfaces through numerical simulation and field tests. The findings demonstrate a favorable association between the normal stress on the joint plane and the stress wave transfer coefficient. The results of the experiments, which were carried out indoors using SHPB equipment by Yu et al. [17], demonstrate that the stress wave's incidence angle will impact the stress wave propagation transmission coefficient in the rock mass filled with joints. Xue et al. [18] conducted triaxial compression and seepage test research on coal under different gas pressures. The mechanical properties, failure process, acoustic emission, and strain energy of coal are analyzed. Xue et al. [19] provided an effective numerical analysis method, which can be used to evaluate the sealing efficiency of the cap layer in underground methane storage. A fully coupled two-phase flow model is established to analyze the migration mechanism of methane in caprock.

The main methods of the above research include theoretical analysis, simulation tests, and physical test research, focusing on the change and influencing factors of stress waves when penetrating joints. In engineering practice, joints generally exist in mining or underground rock mass. However, few studies consider the coupling effect of joint characteristics and stress field. The study shows that the joints under confining pressure can attenuate to a specific extent corresponding to the force waves [20, 21]. As a result, the author considers the qualities of the filling joint material under the joint influence conditions and the coupling impact of various confining pressure levels. The SHPB test device, which can carry out active confining pressure loading on the specimen, is adopted and combined with the numerical simulation method. The stress wave propagation and rock mass fracture characteristics of different joint parameters under active confining pressure are studied. It provides data support for guiding the design of underground protection engineering and the construction of underground facilities.

2. Study on the Effect of Confining Pressure on Stress Evolution and Crushing Behavior of Intact Rock Mass

2.1. Modeling and Parameter Setting. To illustrate the influence mechanism of confining pressure on the loading and unloading characteristics of stress waves in intact rock masses, based on the numerical software LS-DYNA, a three-dimensional model of intact rock mass under 0/3/6/9/12 MPa confining pressure under SHPB impact loading is established. The stress evolution law and crushing behavior effect of intact rock mass under different confining pressure levels are analyzed.

To truly restore the SHPB experimental device in the laboratory test, the 1 : 1 size simulation SHPB device system is used in this numerical modeling. The three-dimensional finite element model is created using the finite element program ANSYS/LS-DYNA. The unit system of cm-g-μs is uniformly used when establishing the model. The incidence rod and transmission rod in the numerical model have 2200 mm and 1800 mm lengths, respectively. The incident rod, transmission rod, and bullet all have a 50 mm diameter. In the numerical model, the HJC model is selected as the constitutive model of rock mass, and its material parameters are shown in Table 1. Figures 1 and 2 demonstrate the system model and the mesh division of rock mass samples, respectively. According to Figure 1, the transmission rod, sample, and incident rod are all arranged from left to right. The system is set to three separate components because the length of the incident rod and transmission rod is inconsistent. Considering that the rock mass material is composed of many

Table 1: Material parameters of HJC constitutive model for sandstone samples.

ρ (kg/m^3)	G (GPa)	A	B	C	N	Fc (MPa)	T (MPa)	E_{ps0}	E_f	S_f
2416	5.16	0.32	1.76	0.007	1	88.3	13.8	2.9×10^6	0.01	5.0
Pc (MPa)	Uc	P_l (GPa)	Ul	D_1	D_2	K_1 (GPa)	K_2 (GPa)	K_3 (GPa)	F_s	
30.45	8×10^4	1.035	0.1	0.045	1	85	-1	208	0.004	

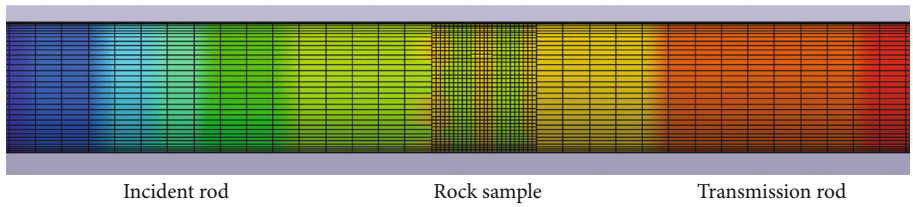

Figure 1: Schematic diagram of the system model.

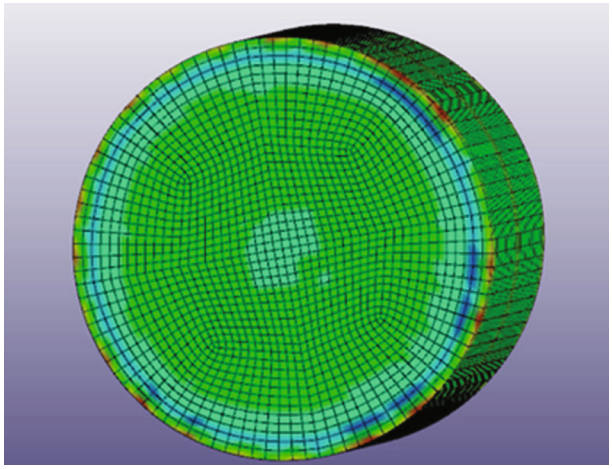

Figure 2: Mesh division of rock mass sample.

mineral particles, the success of the simulation largely depends on the precision of meshing. The spindle-shaped bullet shapes the waveform in this paper. Figure 3 depicts the finite element model.

2.2. Analysis of Numerical Simulation Results. The SHPB test is based on how an elastic stress wave spreads through the bar. Therefore, to ensure the impact simulation test's effectiveness, verifying that the rock mass specimen's internal stress is balanced before failure is crucial. The distribution of the effective internal stress of rock mass specimens at various time nodes and under various confining pressures is shown in Figure 4. The stress wave transmitted from the incident rod to the rock mass specimen will be evenly distributed on the end face of the rock mass specimen, as shown in the figure at $t = 450\,\mu$s. The stress on the end face of various specimens under confining pressure is inconsistent, as is clear from the stress cloud diagram of the end face of the rock mass sample. As shown in the figure $t = 580\,\mu$s, the rock mass specimen reaches the stress equilibrium state, and the stress of each element in the sample is equal. It is obvious that there are obvious cracks in the end face of the specimen, the cracks around the specimen extend further, and the stress failure is not consistent under different confining pressure levels. The figure shows that the internal effective stress distribution of the rock mass specimens under various confining pressure settings is inconsistent at the exact node location. The stress condition of the specimen's end face follows a growing trend and then reduces as the confining pressure rises from 0 MPa to 12 MPa. With the continuous transmission of stress waves, rock mass specimens' end face and internal stress increase gradually.

The failure process of rock mass specimens with various time nodes is depicted in Figure 5 under various confining pressures. It is clear from the failure process that when the loading duration grows from 520 μs to 620 μs and confining pressure increases from 0 MPa to 9 MPa, the end face of the rock mass specimen gradually fails and develops more fractures all around it. However, it can be seen that the specimen's damage level and the number of cracks all around it are both declining as confining pressure is raised to 12 MPa. The final failure effect of specimens under various confining pressures is also erratic, and the degree of damage also tends to initially grow and then subsequently reduce. It demonstrates that the impact resistance of rock can be enhanced within a specific range of confining pressure. However, if the confining pressure continues to increase after reaching a certain peak, the impact resistance of the specimen will decrease.

A comparison of stress-strain curves at various confining pressure levels is shown in Figure 6. The stress-strain curve's general change tendency, which is the pattern of increasing first and then dropping, may be seen in the figure under various confining pressure levels. The confining pressure significantly affects the specimen's stress and strain. The peak stress of the specimen is determined under various confining pressure settings, the data is processed, and the peak stress change curve depicted in Figure 7shows the result. The graphic illustrates how the peak stress of the specimen changes with an increase in confining pressure level, first increasing and then dropping. When the confining pressure is 9 MPa, the peak stress reaches the maximum value of

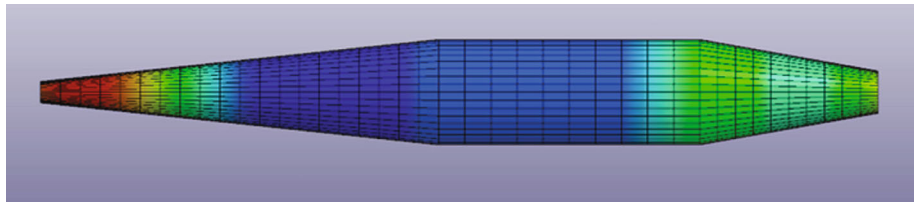

Figure 3: Model diagram of waveform shaping technology.

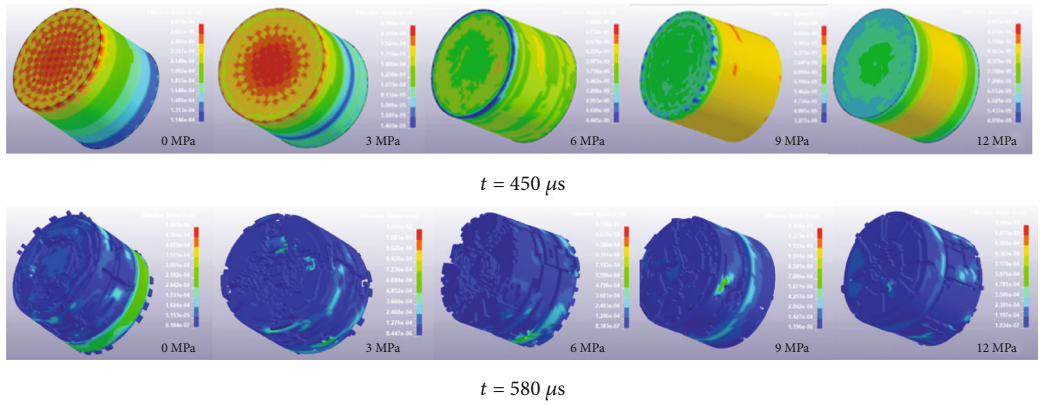

Figure 4: Distribution of effective stress in rock mass samples at different time points.

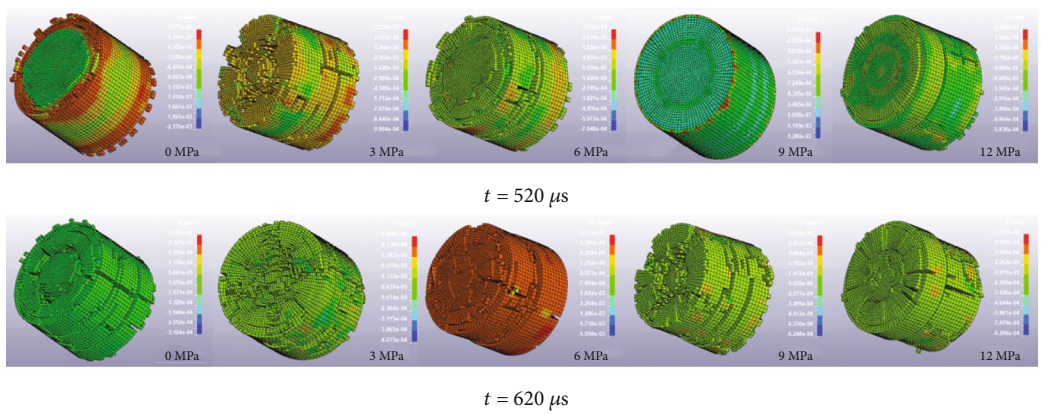

Figure 5: The failure process of the specimen.

88 MPa, which is 21.4% higher than that without confining pressure, and the impact resistance of the specimen is significantly improved. The effect of confining pressure provides a constraint for the specimen, which can effectively restrain the expansion and fracture trend of the specimen under impact load, improve the impact resistance of the rock specimen, and increase the peak impact stress of the specimen. Additionally, the initial microcracks and micropores within the rock specimen tend to close, enhancing the specimen's integrity and increasing its compactness. This results in an improvement in the dynamic compressive strength of the rock specimens. This impact gets more substantial with a rise in confining pressure within a specific range. On the other hand, if the confining pressure level rises above a specific peak range, the microcracks in the specimen will produce significant stress concentration and even induce crack initiation under more significant pressure, causing the specimen's integrity and strength to decline. Therefore, the graph shows that at a pressure of 12 MPa, which is a constricting pressure, the peak stress of the specimen is significantly reduced to 63.7 MPa, which is lower than the peak stress of 72.5 MPa without confining pressure (0 MPa). As can be observed, the above stress and failure damage pattern and the fluctuating peak stress trend are both valid.

Figure 8 shows the reflection and transmission coefficient variation curves with confining pressure. In terms of the overall change trend, the transmission coefficient has a changing trend with an increase in confining pressure that first grows and subsequently decreases. In contrast, the changing trend of the reflection coefficient is the reverse. The shifting pattern indicates that the specimen's stress wave's transmission energy will rise within a range of confining pressure. After reaching a certain peak confining pressure, the transmission energy of the specimen will

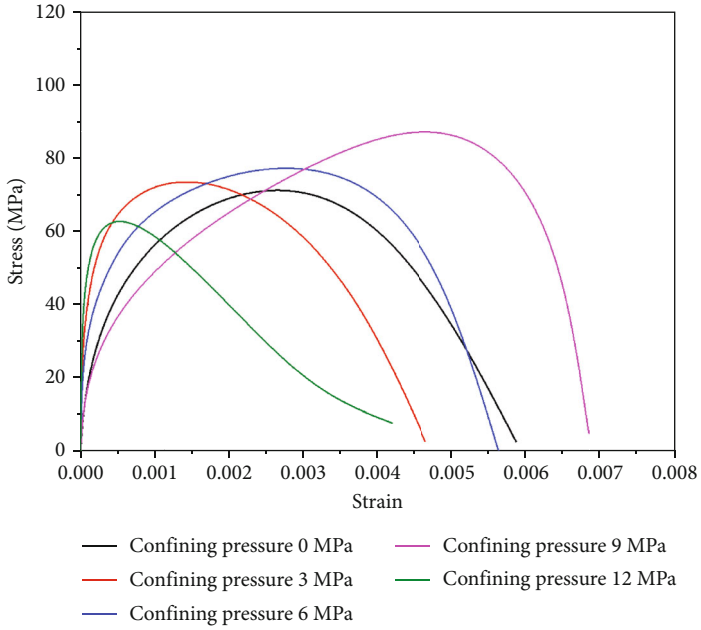

Figure 6: Comparison of stress-strain curves under different confining pressures.

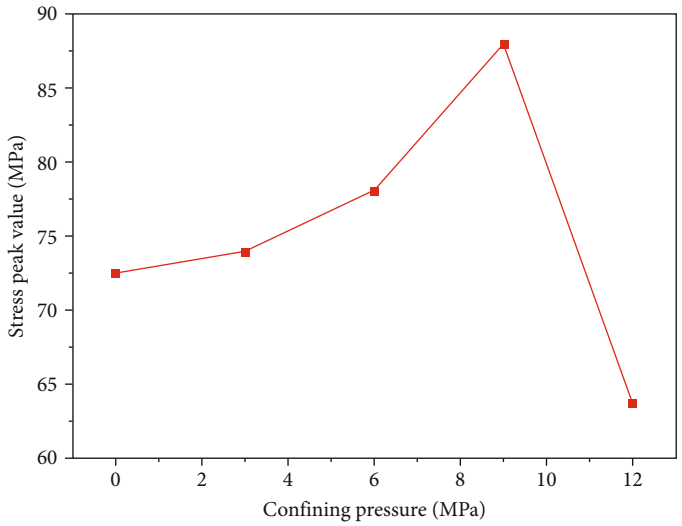

Figure 7: Variation curve of stress peak value with confining pressure.

decrease. However, the reflected energy of the stress wave is opposite to the changing trend of transmission energy. The reflection coefficient achieves its lowest value, and the transmission coefficient reaches its highest value at 9 MPa confining pressure. It demonstrates that the confining pressure rises inside a particular range, gradually strengthening the specimen's constraint and making its interior more compact. To perform work, the incident wave is employed to break the specimen after passing through it. At this time, the transmission coefficient will gradually increase, and the reflection coefficient will gradually decrease. When the confining pressure peaks at a specific value and rises, the reaction will occur, and the specimen's microcracks will result in a substantial stress concentration. They may even crack and fracture when subjected to high pressure. The stress wave is hindered in the process of passing through the specimen, which weakens the transmission ability of the stress wave. At this time, the transmission coefficient will gradually decrease, and the reflection coefficient will gradually increase.

3. Study on the Effect of Joint Materials on Stress Evolution and Crushing Behavior of Jointed Rock Mass

3.1. Test Device. A hydraulic servo testing machine conducts this test, and the test object is the jointed rock mass. The dynamic and static combined loading device is mainly composed of an elastic waveguide rod, guide rod support, base,

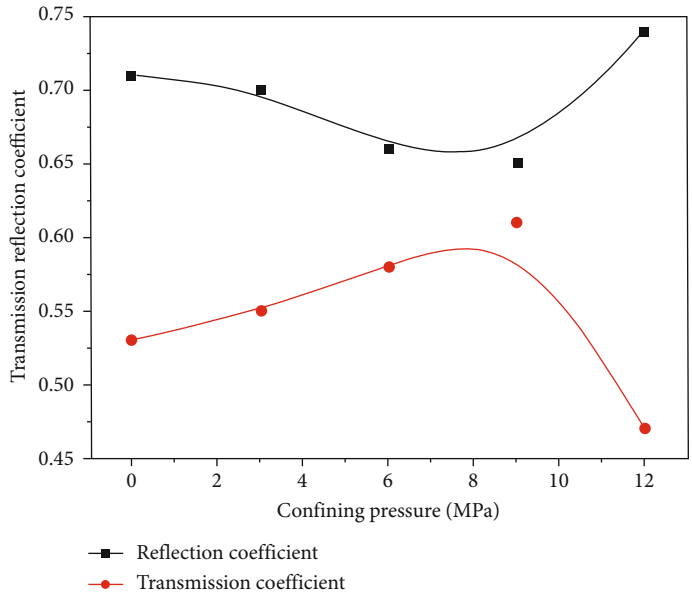

Figure 8: Variation curves of reflection coefficient and transmission coefficient with confining pressure.

stress wave–generating device (gas gun), stress wave measurement sensor, constricting pressure loading apparatus, axial compression loading apparatus, axial compression device bracket, and corresponding measurement and data processing system. The SHPB test system's schematic diagram is shown in Figure 9.

3.2. Impact Test Scheme. The selected bedrock is lime sandstone, and the selected filling materials are gypsum, cement mortar, and epoxy resin. The joint thickness is set to 3 mm, and the joint type is set as through type. The total height of the processed joint specimen is 40 mm, the diameter is 50 mm, and the impact velocity is about 9 m/s. Design and carry out the preparation of joint material specimens. Figure 10 shows the prepared jointed rock mass samples of different joint materials. After the curing of the joint sample is completed, the impact dynamic test performance of the joint sample is tested. The test findings in Table 2 show a substantial relationship between the basic mechanical properties of joint materials and the properties of the materials, and their values are much lower than those of the selected bedrock materials.

3.3. Analysis of Impact Test Results

3.3.1. Specimen Failure Process. Figure 11 shows the final failure effect of specimens of different joint materials after completing the impact test. It can be seen from the crack and damage location in the figure that the dynamic damage results of different joint materials show significant differences. As shown in Figure 11(a), cracks develop in bedrock and joints when the joint material is cement mortar. The joints are subject to crushing damage, accompanied by a certain degree of dust. As shown in Figure 11(b), when the joint material is gypsum, cracks develop in the joints and bedrock under the action of dynamic loads, and cracks with good connectivity are formed. As shown in Figure 11(c), when the joint material is epoxy resin, the jointed rock mass also has an apparent macroscopic failure in dynamic loading. There are only obvious cracks in the joint, and no significant transverse deformation is found.

3.3.2. Properties of the Joint Material Have an Impact on the Dynamic Strength of Jointed Rock Masses. After the impact dynamic test is completed, the dynamic parameters of jointed rock mass under different filling materials are counted, as shown in Table 3. Through the collation and analysis of the data in the table, as shown in Figure 12, it is possible to determine the changing trend of the dynamic strength of jointed rock masses using joint material. From the overall change trend, it has been discovered that changing the joint materials will noticeably alter the dynamic strength of jointed rock mass. When the joint filling materials are cement mortar, gypsum, and epoxy resin, the jointed rock mass test's average dynamic strength is 59.82 MPa, 52.50 MPa, and 22.71 MPa, respectively. From the mechanical test results of the joint materials in Table 2, gypsum, epoxy resin, and cement mortar have uniaxial compressive strengths of 23.77 MPa, 14.33 MPa, and 9.69 MPa, respectively. According to the test results, epoxy resin has the lowest dynamic strength, followed by gypsum and jointed rock masses with cement mortar as the joint medium. The dynamic strength of the jointed rock mass is expected to decline due to the weakening of the joint materials, according to the changing trend of the rock mass's dynamic strength and the test findings of the joint materials' mechanical characteristics.

3.3.3. Variation Law of Transmittance and Reflection Coefficient of Jointed Rock Mass with Joint Material. The reflection coefficient and transmission coefficient can also reflect the variation law of stress wave. Each group of

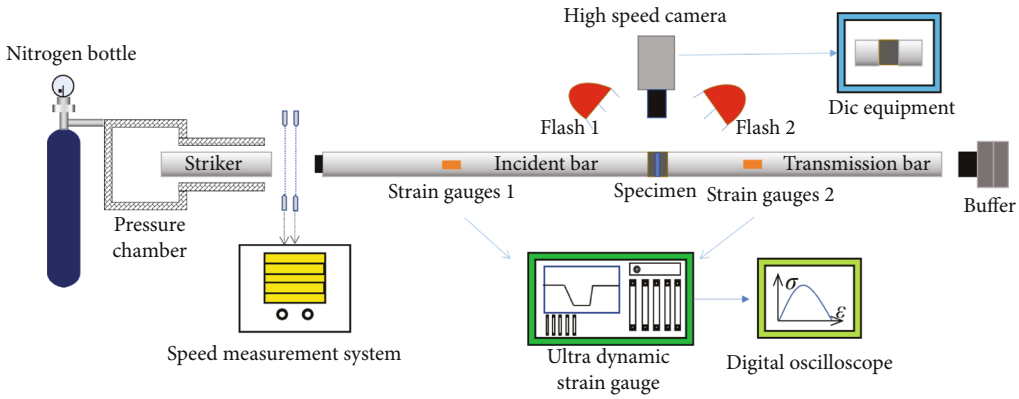

Figure 9: Schematic diagram of the SHPB device.

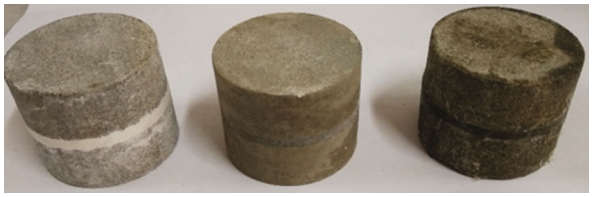

Figure 10: Prepared specimens of different joint materials.

experiments was run three times to guarantee the test's correctness. By sorting out and analyzing the average values of the reflection coefficient and transmission coefficient in Table 3, the variation trend of the transmission coefficient of jointed rock mass with joint materials can be obtained, as shown in Figure 13. Figure 14 depicts the variation trend of the reflection coefficient of a jointed rock mass with joint material. The overall change in the figure shows that the jointed rock mass's transmission coefficient and reflection coefficient show apparent differences with the change of joint material. When the joint materials are cement mortar, gypsum, and epoxy resin, jointed rock mass has average transmission coefficients of 0.44, 0.40, and 0.16, respectively. The transmission coefficient of a jointed rock mass falls as the strength of joint materials decreases, as the transmission coefficient's shifting trend can be observed. When the joint materials are cement mortar, gypsum, and epoxy resin, the average reflection coefficients of the jointed rock mass are 0.77, 0.78, and 0.93, respectively. It may be observed that the reflection coefficient's changing trend is the polar opposite of the transmission coefficients.

3.4. Numerical Simulation Analysis. First, a comparison test of several joint material specimens under the same impact force was conducted to properly perform the comparative test analysis without restricting pressure. Figure 15 shows effective stress distribution in jointed rock mass specimens with different joint materials at the same time node. When $t = 450\,\mu s$, cracks appear in the specimen whose joint material is epoxy resin and gypsum. The middle section of the rock specimen, whose joint material is cement mortar, develops a cross-shaped fissure. The middle piece of the rock specimen, whose joint material is made of gypsum and epoxy resin, develops a crack that resembles a quasicircular form. The stress concentration appears in the center of the rock specimen, whose joint material is epoxy resin. However, there is no crack. With the continuous transmission of stress waves, rock mass specimens' end face and internal stress gradually increase. It can be seen that the final failure degree of different joint materials is also inconsistent. The specimen that uses epoxy resin as the joint substance has the highest degree of crushing. Gypsum was used as the joint material in the specimen, which has the second destructive degree. The specimen covered in cement mortar has the least amount of destruction.

The failure processes of specimens with different joints are compared and analyzed. The failure effect of the specimen demonstrates how inconsistently nodes, failure areas, and cracks are formed by specimens made of various joint materials. The failure process of rock mass specimens is depicted in Figure 16. The end face of the specimen develops a crack along the axis that extends from the center of the end face to the periphery due to the transmission of stress waves and the action of dynamic load on the rock mass specimen. As seen in the figure $t = 510\,\mu s$, epoxy resin exhibits the most significant degree of cracking, followed by gypsum, and cement mortar exhibits the least amount of cracking. With the continuous transmission of stress waves, the specimen gradually transitioned from tensile failure caused by the reflected wave to axial splitting failure. The axial crack along the specimen penetrated the fracture surface. Numerous macroscopic cracks are produced on the specimen along the stress wave's path of propagation, further compressing and reducing the volume of the rock mass specimen. As shown in Figure 16, when $t = 850\,\mu s$, the compression volume of the specimen whose joint material is epoxy resin is the most serious, the cracks in the specimen's cross-section are also the most serious, and the damage to the specimen is also the most serious. When the joint material is gypsum, the damage deformation is the smallest, and the joint material is cement mortar.

In the postprocessing software of numerical simulation, the data of specimens of different joint filling materials under the impact of SHPB are analyzed and sorted out, and the stress-strain curve is drawn. The stress-strain curve

Table 2: Mechanical property parameters of jointed rock mass materials.

Nature	Material name	Compressive strength (MPa)	Elastic modulus (GPa)	Poisson's ratio	Density (g/cm^3)	Longitudinal wave velocity (m/s)
Bedrock	Lime sandstone	84.76	10.96	0.24	2.44	5216.83
	Gypsum	14.33	12.88	0.21	1.75	4977.34
Joint material	Cement mortar	23.77	7.06	0.22	1.81	4740.49
	Epoxy resin	9.69	8.08	0.14	1.10	5016.69

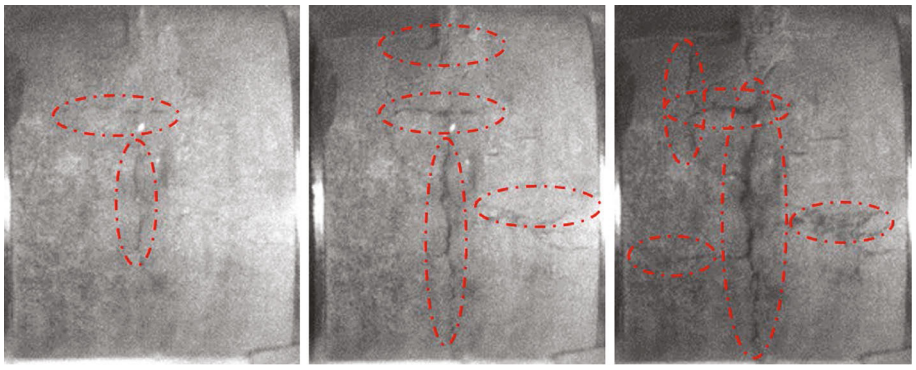

(a) Cement mortar

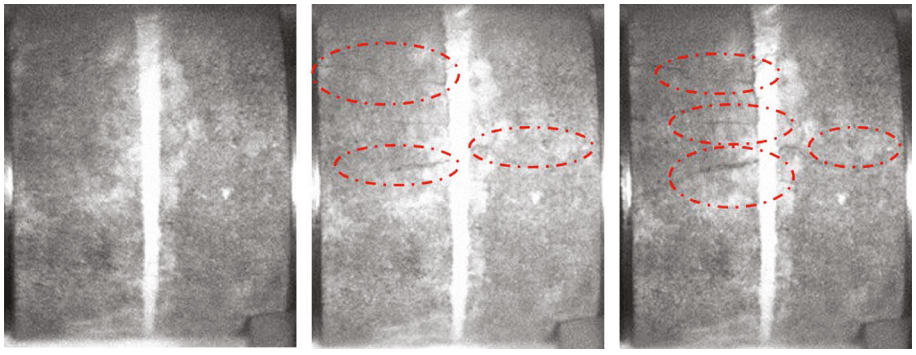

(b) Gypsum

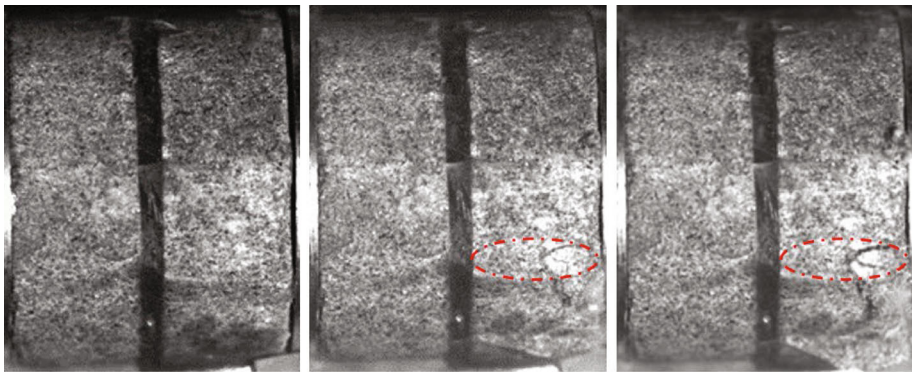

(c) Epoxy resin

Figure 11: Dynamic failure process of specimens with different joint materials.

of the specimen using cement mortar, gypsum, and epoxy resin as joint filling materials has a changing tendency, as illustrated in Figure 17. From the peak stress and the changing trend of the curve, it is clear that the characteristics of joint materials significantly influence the impact stress-strain curve of the entire specimen. Among them, the peak stress of the specimen with cement as joint filling material is the highest, which is 46.2 MPa. Gypsum was used as the joint filling material, which was 44.63 MPa. The epoxy resin is the minor joint filling material, which is 33.1 MPa. The experimental results of the numerical model are consistent with the changing trends and results of the SHPB mentioned

Table 3: Dynamic characteristics of jointed rock mass under the influence of joint material.

Specimen number	Bullet velocity (m/s)	Peak stress (MPa)	Average value (MPa)	Transmission coefficient	Reflection coefficient	Transmission average value	Reflection average value
Gypsum	8.63	57.92	52.50	0.44	0.72	0.40	0.78
	8.67	53.01		0.43	0.66		
	9.20	46.58		0.35	0.85		
Cement mortar	9.42	62.77	59.83	0.46	0.76	0.44	0.77
	9.50	40.83		0.35	0.83		
	9.93	75.90		0.51	0.71		
Epoxy resin	8.71	18.67	22.71	0.15	0.96	0.16	0.93
	8.66	26.89		0.18	0.90		
	8.85	22.56		0.16	0.92		

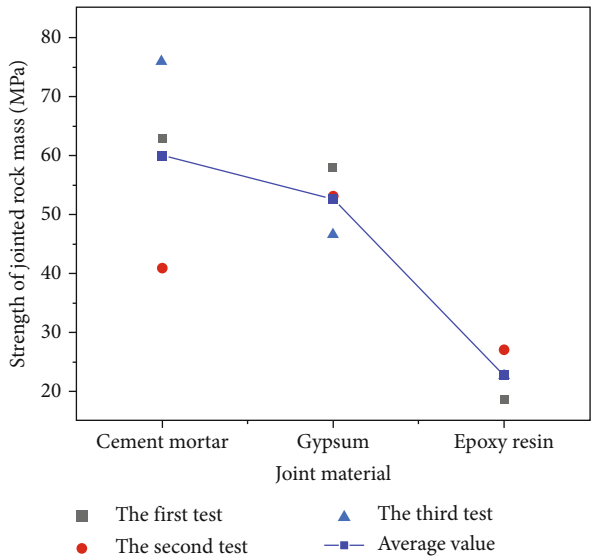

Figure 12: Variation law of jointed rock mass strength with joint material.

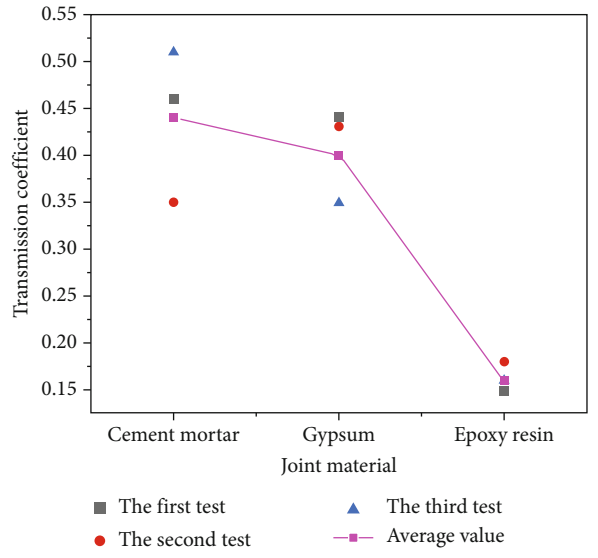

Figure 13: Variation of the transmission coefficient of jointed rock mass with joint material.

above laboratory tests, indicating that the numerical simulation and laboratory tests can verify each other. However, compared with the peak stress of complete rock mass (no joint) specimens, it is clear that the peak stress of the three types of jointed rock mass specimens listed above is considerably lower than the peak stress of specimens of the entire rock mass, indicating that the existence of joints significantly weakens the impact resistance of the specimens and reduces their dynamic compressive strength.

The overall strength of the specimen in the simulation is higher than that in the experimental process because the simulation process is a relatively perfect test system, and the uniformity, stability, and porosity of the simulated materials can be guaranteed. However, there are differences in the test process. Finally, the trend of the simulation's results agrees with the test, proving the simulation's correctness. The failure of the specimen under the same simulation test conditions can start at the center of the specimen section. The section failure area is the smallest when the joint is cement, indicating that the cement and rock mass specimen are fully integrated and their antifailure ability is the greatest. The section failure area of the gypsum joint is the second, which indicates that the joint degree between the gypsum and rock mass specimen is relatively sufficient. The section failure area of the epoxy resin joint is the largest, which indicates that epoxy resin and rock mass specimen cannot form a hole, which seriously affects the impact failure resistance of jointed rock mass.

4. Study on Stress Evolution Law and Crushing Behavior Effect of Jointed Rock Mass under Coupled Confining Pressure and Impact Loading

4.1. Impact Test Scheme. The sandstone is selected as the bedrock rock, and the axial and circumferential confining pressure is 3, 6, and 9 MPa. The joint thickness is 3 mm. The filling material is gypsum, and the joint type is through type. The impact pressure of the impact test is set to two levels, which are 0.2 MPa and 0.5 MPa, respectively. Each impact pressure corresponds to a different impact speed. The impact rod's velocity is around 9 m/s when the impact

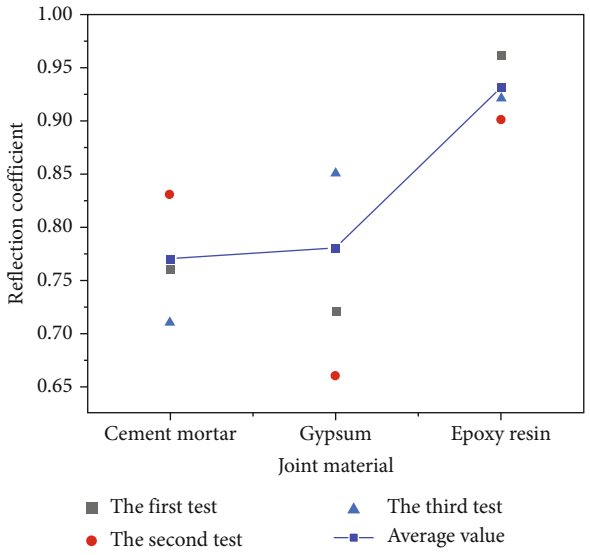

Figure 14: Variation law of reflection coefficient of jointed rock mass with joint material.

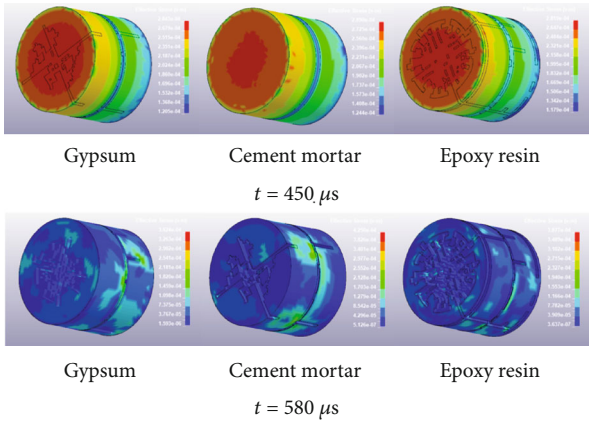

Figure 15: Distribution of effective stress in jointed rock mass specimens with different joint materials at the same time node.

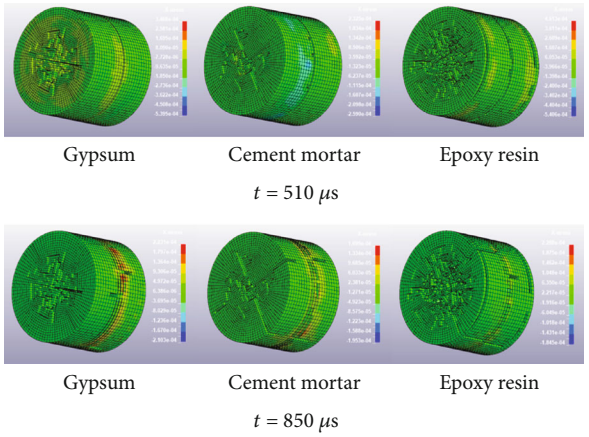

Figure 16: Specimen failure process.

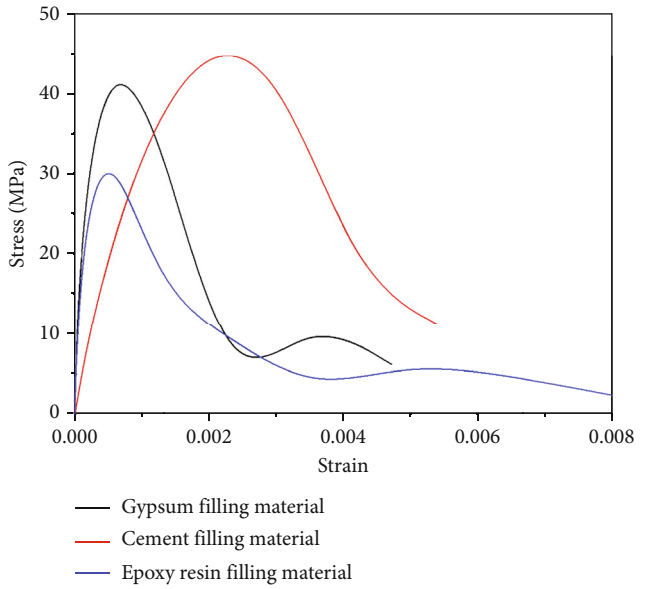

Figure 17: Impact stress-strain curves of specimens with different filling materials.

pressure is set to 0.2 MPa. The impact rod travels at a speed of around 17 m/s when the impact pressure is set to 0.5 MPa.

4.2. Impact Test Results and Analysis

4.2.1. Specimen Failure Mode. The damaging impact on the jointed rock mass specimen is examined once the impact test is complete. Figure 18(a) depicts the failure mode of the jointed rock mass specimen when the impact pressure is 0.2 MPa. It is evident from the specimen's overall failure degree that the jointed rock mass failure primarily occurs in the joint part when the confining pressure is 3 MPa and 6 MPa. The joints are entirely detached from the bedrock, and the joints are destroyed into several large blocks. However, the bedrock is complete without visible damage. The joint only detaches from the bedrock when the confining pressure is 9 MPa, and the impact pressure is applied. No evident damage is done. Compared with the above confining pressure level, the degree of joint failure is decreasing, and the bedrock has no apparent macroscopic failure. The failure pattern of the jointed rock mass specimen illustrated in Figure 18(b) shows that bedrock and joints are damaged with an impact pressure of 0.5 MPa. Under the condition of each confining pressure level, the joints are violently damaged, mainly composed of large blocks and acceptable debris. The failure patterns of bedrock are different under different confining pressures. At 3 MPa and 6 MPa, the confining pressure is minimal, severely damaging the bedrock. The bedrock in contact with one end of the incident rod (marked as the front in Figure 18(b), the same later) and the bedrock in contact with one end of the transmission rod (marked as the back in Figure 18(b), the same later) are significantly damaged. The front bedrock is subject to tensile failure, the fracture plane is parallel to the axial direction, and the rear bedrock is subject to shear failure, which is in the shape of a round table. When the confining pressure is

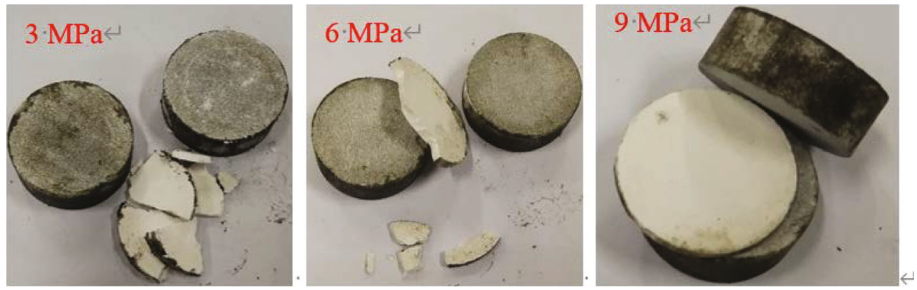

(a) The impact pressure is 0.2 MPa, and the confining pressure is 3, 6, and 9 MPa, respectively

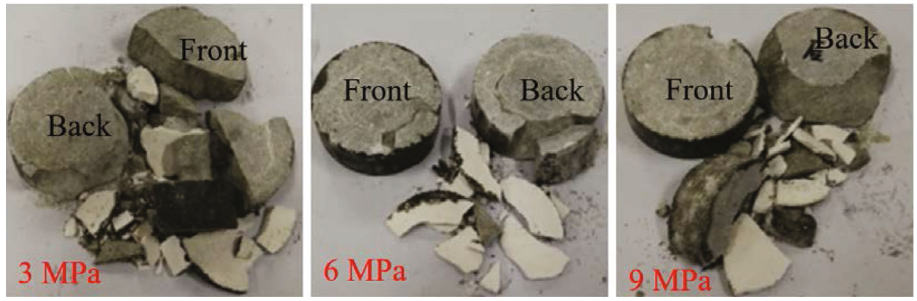

(b) The impact pressure is 0.5 MPa, and the confining pressure is 3, 6, and 9 MPa, respectively

Figure 18: Failure morphology of joint specimen under confining pressure.

9 MPa, the front bedrock has almost no macroscopic failure. However, the rear bedrock is significantly damaged, and its failure form is a round-table shear failure. It demonstrates that the front bedrock will gradually become less damaged under impact pressure as confining pressure rises from 3 MPa to 9 MPa. However, the rear bedrock will continue to have a circular table shape.

4.2.2. The Effect of Active Confining Pressure on Dynamic Strength. After the impact test is completed, the experimental data are statistically analyzed. The two levels of impact pressure correspond to three confining pressure levels. The characteristic dynamic parameters of jointed rock mass obtained from the test are shown in Table 4. The fluctuation in the strength of jointed rock mass with the active confining pressure is depicted in Figure 19 based on the visual analysis of the data in the table. The overall changing trend in the figure demonstrates how the effect of confining pressure dramatically alters the dynamic strength of the jointed rock mass. The dynamic strength of jointed rock mass is positively and linearly proportional to confining pressure within this range. While the impact pressure is 0.2 MPa, the jointed rock mass's dynamic strength is 84.88 MPa when the active confining pressure is 3 MPa. The dynamic strength of jointed rock mass is 105.99 MPa and 115.76 MPa when the active confining pressure is 6 MPa and 9 MPa, respectively, increasing by 24.9% and 36.4%. The stress balance is realized in the dynamic loading process, indicating that the force at both ends of the specimen is the same, which meets the requirements of the dynamic test. When the impact pressure is 0.5 MPa, compared to the impact pressure of 0.2 MPa, under the corresponding three confining pressure levels, the dynamic strength of the jointed rock mass displays a proportional growth trend. The strength of the corresponding jointed rock mass increases by 99.69 MPa, 93.27 MPa, and 94.14 MPa, respectively, for active confining pressures of 3 MPa, 6 MPa, and 9 MPa. It demonstrates that the confining pressure can, up to a point, raise the rock's impact resistance, significantly increase the dynamic strength of the jointed rock mass, and maintain the growth trend.

4.2.3. Variation Law of Transmission and Reflection Coefficient of Jointed Rock Mass with Active Confining Pressure. The reflection and transmission coefficients in the dynamic characteristic parameter table of the jointed rock mass are analyzed by linear regression. Figure 20 depicts the trend of the transmission coefficient of a jointed rock mass under active confining pressure. The active confining pressure is positively associated with the transmission coefficient of the jointed rock mass, as can be observed from the overall change in the figure. The transmission coefficients of the jointed rock mass under the active confining pressure at the 3 MPa levels are 0.51 when the impact pressure is 0.2 MPa. The transmission coefficient of jointed rock mass increases by 29.4% and 41.1%, respectively, when the active confining pressure is at levels of 6 MPa and 9 MPa. These values are 0.66 and 0.72, respectively. The transmission coefficient of the jointed rock mass under the active confining pressure at the 3 MPa level is 0.54 when the impact pressure is 0.5 MPa. The transmission coefficient of jointed rock mass increases by 5.5% and 16.7%, respectively, when the active confining pressure reaches levels of 6 MPa and 9 MPa. These values are 0.57 and 0.63, respectively. By comparing and analyzing the transmission coefficients obtained under two groups of different impact pressure conditions, it is clear that when the impact pressure is high, the jointed rock mass's test-derived transmission coefficients are low. It demonstrates how, with the same constricting pressure, the

Table 4: Dynamic characteristic of jointed rock mass under confining pressure.

Impact pressure (MPa)	Active confining pressure (MPa)	Bullet velocity (m/s)	Peak stress (MPa)	Transmission coefficient	Reflection coefficient
0.2	3	8.65	84.88	0.51	0.77
	6	9.34	105.99	0.66	0.63
	9	9.06	115.76	0.72	0.61
0.5	3	16.95	184.57	0.54	0.92
	6	17.37	199.26	0.57	0.83
	9	17.53	209.90	0.63	0.79

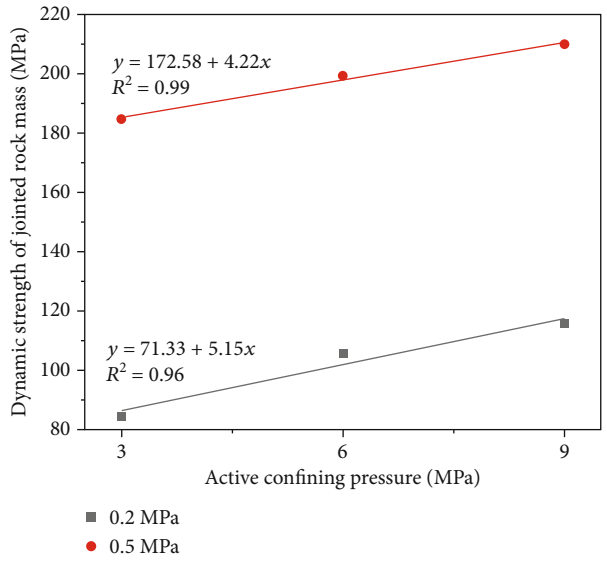

Figure 19: Variation law of jointed rock mass strength with active confining pressure.

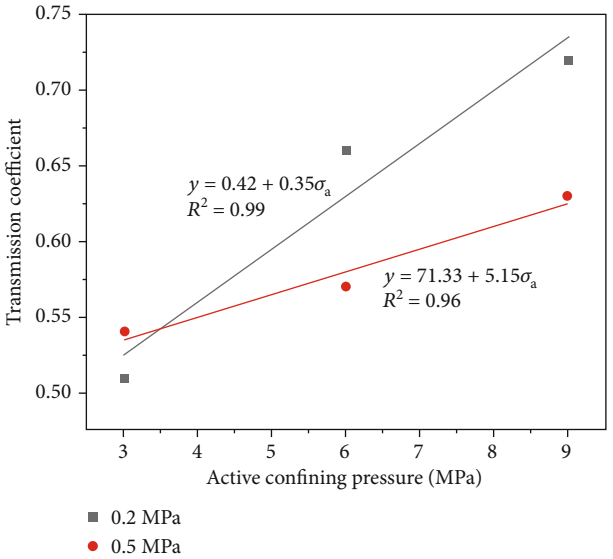

Figure 20: Variation of the transmission coefficient of jointed rock mass with active confining pressure.

proportion of transmitted waves in the jointed rock mass gradually declines as incident energy increases. The linear function is used to fit the active confining pressure and transmission coefficient, and it is found that the correlation coefficient is higher after fitting, both more than 0.9. It shows that the linear variation of active confining pressure and transmission coefficient is significant.

Figure 21 depicts the varying trend of the reflection coefficient of a jointed rock mass with an active confining pressure. The active confining pressure is linearly negatively associated with the jointed rock mass's reflection coefficient, as can be observed from the overall change in the picture. The jointed rock mass's reflection coefficients at the 3 MPa level under the active confining pressure are 0.77 when the impact pressure is 0.2 MPa. The reflection coefficient of jointed rock mass drops by 18.1% and 20.8%, respectively, when the active confining pressure is at 6 MPa and 9 MPa, respectively. These values are 0.63 and 0.61, respectively. The jointed rock mass's reflection coefficient at the 3 MPa levels under the active confining pressure is 0.92 when the impact pressure is 0.5 MPa. When the active confining pressure is at the level of 6 MPa and 9 MPa, the reflection coefficient of the jointed rock mass is 0.83 and 0.79, respectively, which decreases by 9.8% and 14.1%, respectively. By comparing and analyzing the reflection coefficients obtained under two groups of different impact pressure conditions, it is clear that the jointed rock mass generated from the test has high reflection coefficients when the impact pressure is high. It demonstrates how, given constant constriction pressure, the proportion of jointed rock mass reflecting waves steadily rises as incoming energy increases. The linear function is used to fit the active confining pressure and reflection coefficient, and it is found that the correlation coefficient is higher after fitting, both more than 0.9. It shows that the linear variation characteristics of confining pressure and reflection coefficient are relatively significant. The changing trend of the slope of the fitting curve under different confining pressures in the figure is consistent, indicating that the changing trend of the reflection coefficient with the active confining pressure is consistent under different impact pressures.

4.3. Numerical Simulation Analysis. To better carry on the horizontal contrast test analysis, the numerical simulation test of specimens made of various joint materials under the same impact load is conducted under the constraining pressure of 6 MPa. The distribution of the effective internal stress

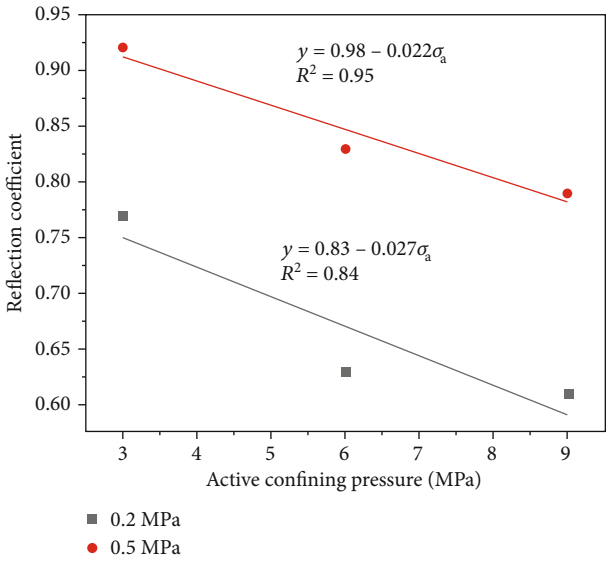

Figure 21: Variation of the reflection coefficient of jointed rock mass with active confining pressure.

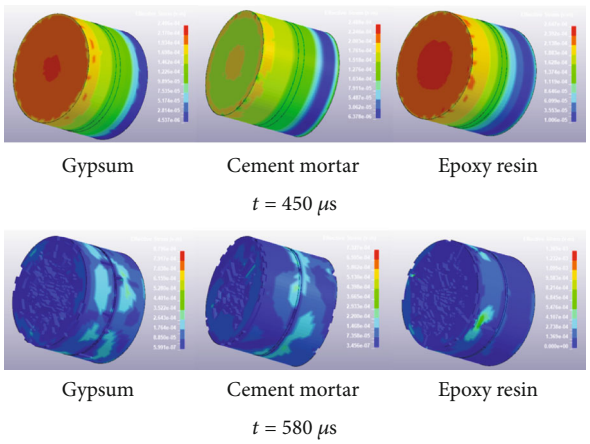

Figure 22: Distribution of effective internal stress of rock mass samples at different time nodes.

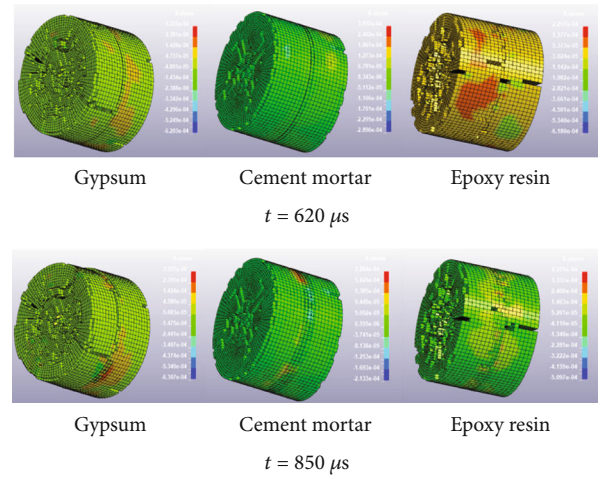

Figure 23: Specimen failure process.

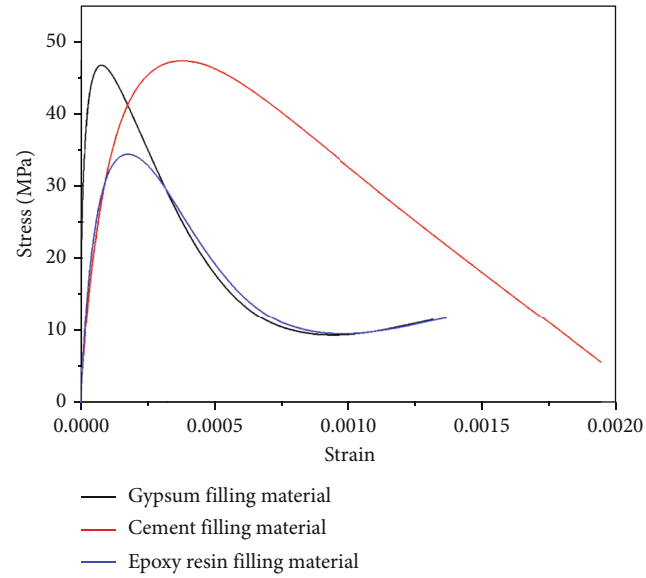

Figure 24: Comparison of stress-strain curves of specimens with different filling materials under the action of confining pressure under SHPB impact.

of rock samples at various time nodes is depicted in Figure 22. The effective stress distribution of various joint materials is similarly uneven at the same time node, as observed from the simulation results' stress cloud diagram. The stress wave transmitted from the incident rod to the rock mass specimen will be evenly distributed across the end face of the rock mass specimen at $t = 450\ \mu s$, as illustrated in the figure. The epoxy resin is under the most stress, followed by gypsum and the cement mortar, according to the stress cloud diagram of the end face of the rock mass sample. With the continuous transmission of stress waves, rock mass specimens' end face and internal stress increase gradually. As shown in the figure $t = 580\ \mu s$, the rock mass specimen reaches a stress equilibrium state at this time, and the stress of each unit in the sample is equal. The end faces and periphery fractures are further stretched and expanded, and the joints in the middle of the specimens of the various joint materials are crushed. It can be seen from the cracks on the end face and surrounding of the rock mass specimen that epoxy resin is subjected to the most significant stress, followed by gypsum, and cement mortar is the smallest.

The failure path of samples made of various joint materials is depicted in Figure 23. It can be seen from the failure process that under the same confining pressure and impact load, the failure effect of different joint material specimens is also inconsistent. When the loading time $t = 620\ \mu s$, it can be seen that cracks appear in the center of the end face of the specimen, and different degrees of peeling damage occur at the center of the end face. It can be seen from the damaging effect that the test piece with epoxy resin as the joint material is the most damaged, the test piece with gypsum is the second most damaged, and the test piece with cement mortar was the least damaged. Many macroscopic cracks are produced in the stress wave's direction as it continues to transmit. As shown in $t = 620\ \mu s$ in the figure, at

this time, the rock gradually transitions from the tension failure caused by the reflected wave to the axial splitting failure, and the axial crack along the specimen penetrates the fracture surface. The volume of the rock specimen is further compressed and reduced, the joint almost disappears, and the final failure effect of the specimen is also consistent with the above.

The stress-strain curves of specimens made of various joint materials under the same impact force are shown in Figure 24. The stress and strain of specimens with various joint materials exhibit a trend of the initial quick rise and subsequent moderate fall in the overall change process. However, there are differences in the peak stress of specimens of different joint materials. Among them, the peak stress of the specimen filled with cement mortar is the highest, which is 50.72 MPa. The peak stress of gypsum is in the middle, 48.4 MPa. The peak stress of epoxy resin is the lowest, 36.52 MPa. The results under the nonconfining pressure condition in the previous work are comparable with the peak stress variation trend of the joint material specimen obtained under the confining pressure condition. In addition, compared with the condition without confining pressure, the peak stress of jointed rock mass specimens with a confining pressure of 6 MPa level increases. It shows that confining pressure can increase the integrity of jointed rock mass to a certain extent and enhance the impact resistance and dynamic compressive strength. Even so, the peak stress of the jointed rock mass specimen under confining pressure is still much lower than that of the intact rock mass. The strengthening effect of confining pressure on the impact resistance of the specimens is much less than the weakening effect of the joints on the impact resistance of specimens.

5. Conclusion

In this paper, based on the two factors of confining pressure level and joint material properties, the influence mechanism of stress wave loading and unloading characteristics and the influence effect of crushing behavior of jointed rock mass are studied and analyzed. Firstly, the numerical simulation of different confining pressure levels for intact rock mass is carried out. Secondly, under the condition of no confining pressure, impact tests were carried out around the properties of joint materials, and corresponding numerical simulation and comparative study were carried out. Finally, a comparative study of impact tests and numerical simulation of jointed rock mass is carried out under coupling confining pressure and impact load. The main conclusions are as follows:

(1) When the confining pressure is within a given range, the entire rock mass's resistance to impacts can be increased. However, the specimen's impact resistance will decrease if the confining pressure rises after reaching a specific peak value. The stress wave in the intact rock mass tends to grow initially before dropping as confining pressure increases simultaneously

(2) The dynamic strength of jointed rock mass decreases with the decrease in the strength of joint materials. For the impact damage resistance, the test piece with epoxy resin as the joint material is the most broken, followed by the test piece with gypsum as the joint material, and the cement mortar as the joint material is the least damaged. With the loss of joint material strength, the stress condition of the stress waves at the same node in a joined rock mass diminishes

(3) The integrity of a jointed rock mass can be improved to some extent by confining pressure, which can also improve impact resistance and dynamic compressive strength. Contrary to popular belief, joints have a significantly more significant strengthening effect on a specimen's impact resistance than confining pressure does

Data Availability

Data are openly available in a public repository.

Conflicts of Interest

The authors declare that they have no conflicts of interest.

References

[1] J. Yu, Q. H. Qian, and X. B. Zhao, "Research progress on effects of structural planes of rock Masson stress wave propagation law," *Acta Armamentarii*, vol. 30, no. S2, pp. 308–316, 2009.

[2] N. S. M. Rezaei and A. P. S. Selvadurai, "Correlation of joint roughness coefficient and permeability of a fracture," *International Journal of Rock Mechanics and Mining Sciences*, vol. 113, no. 1, pp. 150–162, 2019.

[3] M. Y. Wang, Y. T. Zhao, and Q. H. Qian, "Mechanism and quantitative study of seismic isolation effect of slowly dip-angle fractures," *Chinese Journal of Rock Mechanics and Engineering*, vol. 1, pp. 61–65, 1999.

[4] S. B. Chai, J. C. Li, J. H. Zhao, and X. Chen, "Study on stress P-wave propagation across intersecting rock joints with nonlinear deformation," *Chinese Journal of Rock Mechanics and Engineering*, vol. 38, no. 6, pp. 1149–1157, 2019.

[5] W. H. Wang, X. B. Li, Z. L. Zhou, and Y. P. Zhang, "Energy-transmitted rule of various stress waves across open joint," *Journal of Central South University (Science and Technology)*, vol. 2, pp. 376–380, 2006.

[6] M. Ren, D. D. Jiang, W. Huang, and X. S. Li, "Numerical and theoretical analyses of seismic wave response in the non-persistent jointed rock mass," *Acta Seismologica Sinica*, vol. 42, no. 1, pp. 44–52, 2020.

[7] S. W. Lu, H. Y. Liu, J. S. Sun, and C. B. Zhou, "Influence of jointed rockmass on SV wave propagation," *Engineering Blasting*, vol. 26, no. 4, pp. 23–27, 2020.

[8] X. M. Xue, J. Wang, J. Q. Chen, and T. L. Huang, "Influence of structural planes of rock mass on the blasting stress wave," *Metal Mine*, vol. S1, pp. 36–39, 2015.

[9] T. T. Liu, J. C. Li, H. B. Li, and S. B. Chai, "Energy analysis of stress wave propagation across parallel nonlinear joints," *Chinese Journal of Rock Mechanics and Engineering*, vol. 32, no. 8, pp. 1610–1617, 2013.

[10] J. Yu, B. X. Song, and Q. H. Qian, "Propagation of P-waves in dual nonlinear elastic medium for jointed rock mass," *Chinese*

Journal of Rock Mechanics and Engineering, vol. 30, no. 12, pp. 2463–2473, 2011.

[11] L. Song, Z. S. Shao, and M. Z. Wu, "Theoretical analysis on propagation characteristic of stress waves in jointed rock," *Journal of China Coal Society*, vol. 36, no. S2, pp. 241–246, 2011.

[12] L. F. Fan, G. W. Ma, and J. C. Li, "Nonlinear viscoelastic medium equivalence for stress wave propagation in a jointed rock mass," *International Journal of Rock Mechanics and Mining Sciences*, vol. 50, no. 1, pp. 11–18, 2012.

[13] Z. P. Li, W. He, X. Z. Wu, and W. F. Shi, "SHPB tests of the influence of different joint thickness on numerical simulation of stress wave propagation and dynamic behavior of red sandstone," *Journal of Jiangxi University of Science and Technology*, vol. 42, no. 1, pp. 64–73, 2021.

[14] X. P. Li, Q. Dong, T. T. Liu, Y. Luo, H. Zhao, and J. H. Huang, "Model test on propagation of blasting stress wave in jointed rock mass under different in-situ stresses," *Chinese Journal of Rock Mechanics and Engineering*, vol. 35, no. 11, pp. 2188–2196, 2016.

[15] X. C. Zhao, X. Y. Zhao, and J. Q. Guo, "Experimental study on acoustic and mechanical properties of intermittent jointed rock mass," *Chinese Journal of Rock Mechanics and Engineering*, vol. 39, no. 7, pp. 1408–1419, 2020.

[16] T. T. Liu, J. C. Li, H. B. Li, X. P. Li, Y. Zheng, and H. Liu, "Experimental study of S wave propagation through a filled rock joint," *Rock Mechanics and Rock Engineering*, vol. 50, no. 10, pp. 2645–2657, 2017.

[17] J. Yu, Z. H. Liu, Z. He, X. Q. Zhou, and J. B. Ye, "Fluctuation characteristic test of oblique stress waves in infilled jointed rock and study of the analytic method," *Advances in Civil Engineering*, vol. 2020, Article ID 7924742, 12 pages, 2020.

[18] Y. Xue, P. G. Ranjith, F. Gao, Z. Zhang, and S. Wang, "Experimental investigations on effects of gas pressure on mechanical behaviors and failure characteristic of coals," *Journal of Rock Mechanics and Geotechnical Engineering*, vol. 15, no. 2, pp. 412–428, 2023.

[19] Y. Xue, S. Liu, J. Chai et al., "Effect of water-cooling shock on fracture initiation and morphology of high-temperature granite: Application of hydraulic fracturing to enhanced geothermal systems," *Applied Energy*, vol. 337, 2023.

[20] X. Yang, C. J. Pu, T. Liao, and D. J. Xiao, "Influence of prefabricated cracks with different fillers on explosive crack propagation," *Explosion and Shock Waves*, vol. 36, no. 3, pp. 370–378, 2016.

[21] X. J. Feng, Q. M. Zhang, and A. Muhammad, "Explosion-induced stress wave propagation in interacting fault system: numerical modeling and implications for Chaoyang coal mine," *Shock and Vibration*, vol. 2019, Article ID 5856080, 12 pages, 2019.